GEOPHYSICS, VOL. 75, NO. 4 (JULY-AUGUST 2010); P. F115–F126, 9 FIGS.
10.1190/1.3473694

3D time-domain simulation of electromagnetic diffusion phenomena: A finite-element electric-field approach

Evan Schankee Um[1], Jerry M. Harris[1], and David L. Alumbaugh[2]

ABSTRACT

We present a finite-element time-domain (FETD) approach for the simulation of 3D electromagnetic (EM) diffusion phenomena. The finite-element algorithm efficiently simulates transient electric fields and the time derivatives of magnetic fields in general anisotropic earth media excited by multiple arbitrarily configured electric dipoles with various signal waveforms. To compute transient electromagnetic fields, the electric field diffusion equation is transformed into a system of differential equations via Galerkin's method with homogeneous Dirichlet boundary conditions. To ensure numerical stability and an efficient time step, the system of the differential equations is discretized in time using an implicit backward Euler scheme. The resultant FETD matrix-vector equation is solved using a sparse direct solver along with a fill-in reduced ordering technique. When advancing the solution in time, the FETD algorithm adjusts the time step by examining whether or not the current step size can be doubled without unacceptably affecting the accuracy of the solution. To simulate a step-off source waveform, the 3D FETD algorithm also incorporates a 3D finite-element direct current (FEDC) algorithm that solves Poisson's equation using a secondary potential method for a general anisotropic earth model. Examples of controlled-source FETD simulations are compared with analytic and/or 3D finite-difference time-domain solutions and are used to confirm the accuracy and efficiency of the 3D FETD algorithm.

INTRODUCTION

Transient electromagnetic (TEM) methods have been extensively used in applied geophysics. Because interpretations of TEM data in complex geologic environments increasingly must resort to forward and inverse modeling, the forward numerical simulation of the TEM fields is of particular interest. Introduced by Yee (1966) and Taflove (1980) in engineering computational electromagnetics, finite-difference time-domain (FDTD) algorithms have become one of the standard tools used to simulate TEM methods. Their popularity is due to the fact that FDTD methods are relatively straightforward to implement, highly efficient, and able to provide accurate solutions over a wide range of TEM simulations.

Among the variety of FDTD algorithms, the most popular one is probably a 3D FDTD algorithm coupled with a staggered-grid technique and the Du Fort-Frankel method (Wang and Hohmann, 1993). As geophysics research has resorted increasingly to larger and larger models, this particular FDTD algorithm has been translated into parallel versions (Commer and Newman, 2004). The parallel version provides two additional algorithmic features: (1) computation of the initial electric field responses over arbitrary conductivity distributions via a 3D finite-difference Poisson solver, and (2) support for an arbitrarily oriented, finite-long electric dipole source. In short, these new features make it possible to simulate the TEM response to more realistic earth models than previously.

Although the 3D FDTD algorithm has enjoyed considerable popularity, it also has well-known drawbacks. Its practical weakness is that large, complex geologic structures (e.g., topography, bathymetry, and heterogeneity), which do not conform to rectangular grids, need to be captured by a stair-step approximation. The stair-step approximation might seem to adequately model significant irregularity using a series of very small grids in parallel-computing environments. However, such stair steps can introduce errors into numerical modeling results, especially when sources and receivers are placed on or very close to the complex surface described by the stair steps. Furthermore, the stair-step modeling approach can introduce unnecessarily small grid spacing, resulting in an inefficiently small time-step size in the Du Fort-Frankel method.

We implement a finite-element time-domain (FETD) solver for diffusive EM simulation in complex geologic environments. In contrast to FDTD methods, FETD methods are based on a geometry-conforming unstructured mesh that allows precise representations of arbitrarily irregular topography and complex geologic structures in a

Manuscript received by the Editor 29 October 2009; revised manuscript received 14 February 2010; published online 31 August 2010.
[1]Stanford University, Department of Geophysics, Stanford, California, U.S.A. E-mail: evanum@gmail.com; jerry.harris@stanford.edu.
[2]Schlumberger-EMI Technology Center, Richmond, California, U.S.A. E-mail: dalumbaugh@slb.com.

computationally elegant way. In addition, the unstructured mesh easily enables more accurate modeling of subtle geometric changes in a region (e.g., geologic CO_2 storage in a monitoring environment or a hydrocarbon reservoir in a production environment), isolating the true TEM perturbation caused by the target itself. Such an accurate electromagnetic (EM) simulation is critical for imaging and inversion problems, especially for improving the detection and monitoring of targets that generate small anomalous signals.

Compared with FDTD methods, the adoption of FETD methods for EM wave and diffusion problems was rather slow to take hold in engineering EM and geophysical EM literature. One theoretical reason for this is that node-based finite-element (FE) methods do not correctly represent the discontinuity of normal field components at material interfaces. This problem was solved with the introduction of edge-based elements that correctly represent the discontinuities of EM fields at the interfaces (Nédélec, 1980, 1986; Bossavit, 1988). The FETD methods also are less popular because they generally require solving a matrix-vector equation at every time step regardless of implicit or explicit time discretization (Gockenbach, 2002). Therefore, for a given number of unknowns, this aspect makes FETD methods computationally more expensive than explicit FDTD methods. However, the advent of powerful computers and efficient numerical linear algebra libraries has alleviated the problem and made the FETD problems increasingly tractable.

Various FETD formulations for EM simulations have been developed using different forms of EM equations: coupled Maxwell's equations, scalar and vector potentials with a gauge condition, and the electric field wave equation (Biro and Preis, 1989; Lee et al., 1997; Jin, 2002; Taflove and Hagness, 2005). Although the equations equivalently describe EM phenomena, each has its own advantages and disadvantages in the implementation of the FETD (Zhu and Cangellaris, 2006). In this study, we choose an FETD formulation of the electric field full-wave equation (Gedney and Navsariwala, 1995) as our starting point, and migrate to its diffusion version. Although it is beyond the scope of our paper to provide detailed comparisons of the different formulations, the primary advantage of the FETD formulation over others is the fact that we need to consider only the electric fields as our primary unknowns, thus minimizing the total number of parameters to solve.

We propose an FETD-solution approach for an exploration-scale diffusion problem. The development of its FETD formulation is close to that of wave and/or eddy current problems which have been broadly investigated in engineering computational electromagnetics (Cangellaris et al., 1987; Gedney and Navsariwala, 1995; Lee et al., 1997; Rieben and White, 2006). However, the implementation details of the formulation in the exploration-scale diffusion domain are considerably different from those especially in terms of time stepping, boundary conditions, and mesh design.

Our FETD implementation is also distinguished from other exploration-scale FETD solutions in some important aspects. First, we compute FETD solutions directly in the time domain, whereas other published methods (e.g., Everett and Edwards, 1992; Börner et al., 2008) use the transform of finite-element frequency-domain solutions. With a step-off source, our direct time-domain approach requires that we calculate the initial electric fields; we do this using Poisson's equation before time stepping. At least as far as we know, the direct time-domain computation with the finite-element method in the diffusion domain has never appeared in the geophysics literature.

Second, in the direct time-domain computation, the primary computational cost is time stepping, which requires the solution of a matrix equation at every time step. To mitigate the computational cost, we reuse sparse LU factorization of the matrix equation unless a time-step size is changed. As a result, the computational cost at most time steps reduces to that of back and forward substitution of a sparse matrix equation. Third, by exploiting the phenomena of EM attenuation, we adaptively double a time-step size to speed up solution processes over a large range of time. As demonstrated in this study, this time-stepping approach helps to avoid impractical small changes of a time-step size that would result in expensive LU factorizations.

Finally, we combine our FETD with a secondary potential FE solution, whereas Commer and Newman (2004) incorporate their FDTD with a total potential finite-difference solution. The adoption of the secondary potential method considerably improves the accuracy of the initial electric fields required for step-off simulations. The accurate computation of the initial electric fields is critically important in step-off simulations because inaccurate initial electric fields can result in errors such as static shift of TEM sounding curves. This type of error is difficult to identify because the error does not change the overall shape of the sounding curves.

Our paper is organized as follows. First we review the development of a system of differential equations that approximates the solution of the full electric field wave equation and migrates to its diffusion version. Then, we discretize the system in temporal and spatial domains, and transform it into the final 3D FETD formulation. We describe herein two important aspects of the 3D FETD implementation: boundary conditions and initial conditions. Then our numerical solution strategies for the FETD formulation are presented in detail. We validate the 3D FETD algorithm through detailed comparison with 1D analytic and 3D FDTD simulation results, and present a performance analysis of the FETD algorithm. Finally, using our 3D FETD algorithm, we present simulation results of the time-domain controlled-source electromagnetic (TD-CSEM) method for a simple field scenario of a water layer above a gently dipping seafloor.

NUMERICAL SOLUTION APPROACH

In this section, we start from an FETD development of the full electric field wave equation (Gedney and Navsariwala, 1995). In a given computational domain $\mathbf{V}$, the electric field wave equation is given as

$$\nabla \times \left[\frac{1}{\mu} \nabla \times \mathbf{e}(\mathbf{r},t) \right] + \bar{\bar{\boldsymbol{\varepsilon}}} \frac{\partial^2 \mathbf{e}(\mathbf{r},t)}{\partial t^2} + \bar{\bar{\boldsymbol{\sigma}}} \frac{\partial \mathbf{e}(\mathbf{r},t)}{\partial t} = - \frac{\partial \mathbf{j}_s(\mathbf{r},t)}{\partial t}, \tag{1}$$

where $\mathbf{e}(\mathbf{r},t)$ is the electric field at time t at position $\mathbf{r} \in \mathbf{V}$; μ, $\bar{\bar{\varepsilon}}$, $\bar{\bar{\boldsymbol{\sigma}}}$, and $\mathbf{j}_s(\mathbf{r},t)$ are the magnetic permeability, the 3×3 dielectric permit-

tivity tensor, the 3×3 symmetrical electric conductivity tensor, and the electric current source term, respectively.

To transform equation 1 into an FETD approximate equation, a residual vector $\mathbf{p}$ is defined as

$$\mathbf{p}(\mathbf{r},t)\equiv\nabla\times\left[\frac{1}{\mu}\nabla\times\mathbf{e}(\mathbf{r},t)\right]+\bar{\bar{\varepsilon}}\frac{\partial^2\mathbf{e}(\mathbf{r},t)}{\partial t^2}+\bar{\bar{\sigma}}\frac{\partial\mathbf{e}(\mathbf{r},t)}{\partial t}+\frac{\partial\mathbf{j}_s(\mathbf{r},t)}{\partial t}. \quad (2)$$

The $\mathbf{V}$ is discretized into a number of finite elements. The residual vector for each element is forced to be zero in a weighted-integral sense. Among several shapes of finite elements, a tetrahedral element is chosen because the tetrahedral form can efficiently handle complex geometry. This process is expressed as the following equation:

$$\int\int\int_{V^e}\mathbf{n}_i^e(\mathbf{r})\cdot\mathbf{p}^e(\mathbf{r},t)dV=0, \quad (3)$$

where the superscript e denotes the eth tetrahedral element, $\mathbf{n}_i^e(\mathbf{r})$ is a set of weighting functions with i varying from 1 to n, and V^e is the volume of the eth tetrahedral element.

If the set of $\mathbf{n}_i^e(\mathbf{r})$ functions used in equation 3 is also chosen as the basis set, the electric field is expanded as

$$\mathbf{e}^e(\mathbf{r},t)=\sum_{j=1}^{n}\mathbf{e}_j^e(\mathbf{r},t)=\sum_{j=1}^{n}u_j^e(t)\mathbf{n}_j^e(\mathbf{r}), \quad (4)$$

where $u_j^e(t)$ is the unknown amplitude of the electric field on edge j of the eth element that needs to be determined via FETD computations. In the application of Galerkin's method to EM modeling, edge-based functions (Whitney, 1957) are chosen as basis functions. The functions guarantee both the tangential continuity and normal discontinuity of the expanded electric field across the element edges. In equations 3 and 4, we set $\mathbf{n}^e(\mathbf{r})$ to the first-order edge-based functions. More details on the properties of the basis functions are provided by Jin (2002) and Taflove and Hagness (2005), as well as by the references cited in the Introduction.

Substituting equation 4 into equation 3 provides the following system of second-order ordinary differential equations:

$$\mathbf{A}^e\frac{d^2\mathbf{u}^e(t)}{dt^2}+\mathbf{B}^e\frac{d\mathbf{u}^e(t)}{dt}+\mathbf{C}^e\mathbf{u}^e(t)+\mathbf{s}^e=0, \quad (5)$$

where the (i,j) element of matrices $\mathbf{A}^e$, $\mathbf{B}^e$, and $\mathbf{C}^e$, and the ith element of vectors $\mathbf{s}^e$ and $\mathbf{u}^e$, are given by the following:

$$(i,j)\text{ element of }\mathbf{A}^e=\int\int\int_{V^e}\bar{\bar{\varepsilon}}^e\mathbf{n}_i^e(\mathbf{r})\cdot\mathbf{n}_j^e(\mathbf{r})dV; \quad (6)$$

$$(i,j)\text{ element of }\mathbf{B}^e=\int\int\int_{V^e}\bar{\bar{\sigma}}^e\mathbf{n}_i^e(\mathbf{r})\cdot\mathbf{n}_j^e(\mathbf{r})dV; \quad (7)$$

$$(i,j)\text{ element of }\mathbf{C}^e=\int\int\int_{V^e}\frac{1}{\mu}\nabla\times\mathbf{n}_i^e(\mathbf{r})\cdot\nabla\times\mathbf{n}_j^e(\mathbf{r})dV; \quad (8)$$

$$i\text{ element of }\mathbf{s}^e=\int\int\int_{V^e}\mathbf{n}_i^e(\mathbf{r})\cdot\frac{\partial\mathbf{j}_s(\mathbf{r},t)}{\partial t}dV; \quad (9)$$

$$\mathbf{u}^e=[u_1^e,u_2^e,\ldots,u_n^e]. \quad (10)$$

Diffusive EM domain

In equation 5, the first term is related to the EM displacement current. Because the displacement current is much smaller than the conduction current in the low-frequency EM diffusion regime, this first term is negligible and can be dropped. By dropping the term, the finite velocity of the EM fields in the perfectly resistive medium (e.g., air) is replaced by an infinite velocity (Goldman et al., 1985). However, the change in the velocity of the airwave does not affect an EM geophysical simulation result because of its relatively short source-receiver offset compared with the true wavelength of the airwave. In this regime, equation 5 eventually reduces to a system of diffusion equations. The system of equations is considered local because it results from integration over each individual tetrahedral element. Based on connectivity information about tetrahedral elements in $\mathbf{V}$, the local systems of diffusion equations assembled for the individual elements are assembled into a single global system as shown below:

$$\mathbf{B}\frac{d\mathbf{u}(t)}{dt}+\mathbf{C}\mathbf{u}(t)+\mathbf{s}=0. \quad (11)$$

Discretization in time and space

Because equation 11 is a time-dependent system of ordinary differential equations, it can be discretized in time using a finite-difference (FD) method. To choose an effective FD method, we must consider the physics of EM diffusion problems. Due primarily to the low-frequency EM sources we wish to simulate and the large contrast in electrical conductivity between the subsurface medium and air, equation 11 is very stiff in time (Haber et al., 2004). Therefore, if we choose an explicit time-discretization method, equation 11 will require a very small time step Δt to satisfy stability conditions. For this reason, an explicit time-discretization method would not be efficient, especially when TEM responses need to be simulated over a large range of time (e.g., from 10^{-6} to 10^{2} s) in conductive environments.

Thus, we choose implicit time discretization, the backward Euler (BE) method. As an implicit method, the BE method is unconditionally stable regardless of the choice of Δt. Furthermore, when a mesh cannot handle high-frequency contents of the transient source pulses in early time, the BE method strongly suppresses high-frequency oscillations (Hairer and Wanner, 1991). The accuracy of the BE method is set to second order for somewhat complex source waveforms (e.g., a Gaussian and half-sine waveform) and first order for a simple step-off and step-on source waveform. The latter is due to the fact that there is no benefit of using a higher order scheme for a source

waveform that is only once differentiable (Haber et al., 2004). Applying the BE method to equation 11 produces

$$\mathbf{D}\mathbf{u}^{n+2} = \mathbf{B}(4\mathbf{u}^{n+1} - \mathbf{u}^{n}) - 2\Delta t\mathbf{s}^{n+2}$$

for the second-order BE method, (12a)

where $\mathbf{u}(t) = \mathbf{u}(n\Delta t) = \mathbf{u}^n$ and $\mathbf{D} = (3\mathbf{B} + 2\Delta t\mathbf{C})$; and

$$\mathbf{D}u^{n+1} = \mathbf{B}u^{n} - \Delta t\mathbf{s}^{n+1} \text{ for the first-order BE method,} \quad (12b)$$

where $\mathbf{D} = (\mathbf{B} + \Delta t\mathbf{C})$.

For the solution of equations 12a and 12b to approximate true electric fields accurately, the spatial discretization of the computational domain is as important as the temporal discretization. As a general rule for the spatial discretization, an element size is smallest near a source and gradually grows away from the source (Wang and Hohmann, 1993). The growth rate is empirically determined but is usually less than or equal to a factor of two from one edge to the next. In addition, the mesh should be fine in conductive areas, but it can be coarse in more resistive areas (Hördt and Müller, 2000). Such a mesh design is illustrated in Figure 1, and makes it possible to impose Dirichlet boundary conditions on external edges of a model, as discussed below. In short, the finite-element mesh must consider model inhomogeneity as well as diffusion and attenuation characteristics of transient EM fields with time.

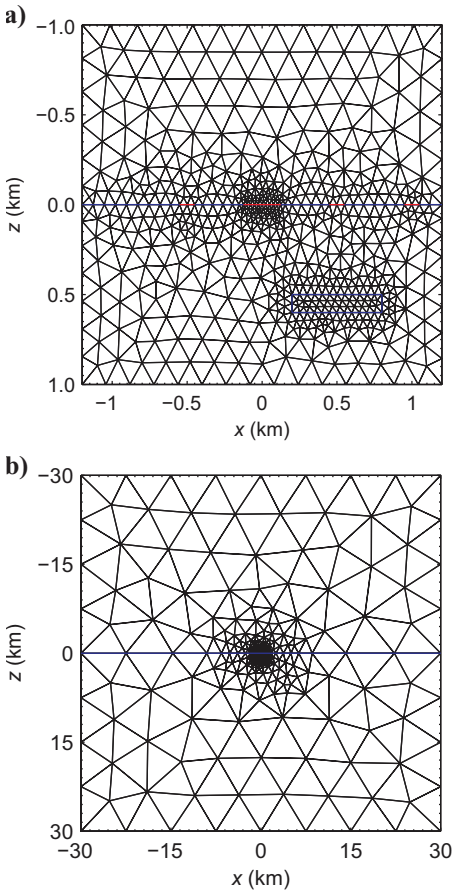

Figure 1. A cross-sectional (2D) view ($y = 0$ m) of the 3D FETD mesh used for a 3D gas reservoir model shown in Figure 6. (a) The central portion of the cross section. (b) The entire view of the cross section. The air-earth interface that bisects the cross-sectional view is colored blue. In (a), the blue rectangular box represents a reservoir. The red-colored line segment at the center of the mesh is a finite-long electric dipole source. The other small red-colored line segments on the air-earth interface are receivers.

Boundary conditions

To obtain a unique numerical solution for a given differential equation, geophysically meaningful conditions need to be imposed at the boundaries of the computational domain. Because element sizes can grow with increasing offset from a source position, we extend the boundaries of an earth model sufficiently away from the source. Then homogeneous Dirichlet boundary conditions are applied to the FETD matrix-vector equation by setting the electric fields on the external edges to zeros and removing the edges from the matrix-vector equation. As a result, the number of unknowns in equations 12a and 12b reduces from the number of total edges to that of internal edges. We believe that the homogeneous Dirichlet boundary condition is the most practical choice for EM diffusion simulations because its implementation does not require modifying the original form of the governing equation, nor does it result in any extra computation at each time step. Our numerical experiments also suggest that in most earth models, the number of elements required for such a mesh design does not significantly increase the total number of elements when a proper element growth rate is chosen.

Initial conditions

To advance the solution of equations 12a and 12b, we first need to set up the initial electric field. When an earth model is excited using a step-on, half-sine, or Gaussian source waveform, the initial electric field is zero everywhere in the model. However, when a step-off source waveform is used, the initial electric field is not zero but a solution of the direct current (DC) resistivity problem. In this case, the initial electric field can be decomposed into two parts (Commer and Newman, 2004):

$$\mathbf{e}_{\text{initial}} = \mathbf{e}_{\text{source}} + \mathbf{e}_{\text{DC}}, \quad (13)$$

where $\mathbf{e}_{\text{initial}}$ is the initial electric field vector, $\mathbf{e}_{\text{source}}$ is the electric field through a source, and $\mathbf{e}_{\text{DC}}$ is the DC electric field in the model, respectively.

The electric field $\mathbf{e}_{\text{source}}$ is determined by applying Ohm's law to the tetrahedral elements containing the source. The electric field $\mathbf{e}_{\text{DC}}$ is determined by calculating electric potentials at the nodes of the finite elements; the calculation reduces to a 3D Poisson problem, as is common in 3D resistivity modeling (Dey and Morrison, 1978; Lowry et al., 1989; and Li and Spitzer, 2002). We solve the 3D Poisson's equation for general anisotropic media using a secondary potential approach (Li and Spitzer, 2005). Compared with the total potential approach, the secondary potential approach considerably improves the solution accuracy in the vicinity of a source by removing the singularity. As a result, the secondary potential approach effectively prevents numerical static shift errors in step-off sounding curves.

To maintain consistency in the development procedures of the previous FE formulation, the finite-element DC (FEDC) formulation is summarized below using a weighted residual method instead of a variational principle. The DC resistivity problem is described with the Poisson's equation

$$\nabla \cdot (\bar{\bar{\sigma}} \nabla \phi(\mathbf{r})) = -\nabla \cdot \mathbf{j}_s(\mathbf{r}), \tag{14}$$

where $\phi(\mathbf{r})$ is a potential at position $\mathbf{r}$. The potential is decomposed into a primary potential $\phi_p(\mathbf{r})$ and secondary potential $\phi_s(\mathbf{r})$:

$$\phi(\mathbf{r}) = \phi_p(\mathbf{r}) + \phi_s(\mathbf{r}). \tag{15}$$

The primary potential is caused by the current source in a homogeneous whole space with the primary conductivity tensor $\bar{\bar{\sigma}}_p$, and it can be calculated analytically at the FE nodes. The secondary potential satisfies the following equation:

$$\nabla \cdot (\bar{\bar{\sigma}}_s \nabla \phi_s(\mathbf{r})) = -\nabla \cdot \mathbf{j}_s(\mathbf{r}), \tag{16}$$

where $\bar{\bar{\sigma}}_s = \bar{\bar{\sigma}} - \bar{\bar{\sigma}}_p$.

As done before, a scalar residual for the eth tetrahedron is defined as

$$\mathrm{p}^e(\mathbf{r}) = \nabla \cdot (\bar{\bar{\sigma}}_s \nabla \phi_s(\mathbf{r})) + \nabla \cdot \mathbf{j}_s(\mathbf{r}). \tag{17}$$

The residual for each tetrahedral element is minimized in a weighted average sense

$$\int\int\int_{V^e} \omega(\mathbf{r}) \mathrm{p}^e(\mathbf{r}) dv = 0, \tag{18}$$

where $\omega(\mathbf{r})$ is a weighting function.

By substituting equation 17 into equation 18, using Green's theorem and finally enforcing Dirichlet boundary conditions, one can easily obtain

$$\begin{aligned}
&\int\int\int_{V^e} \left[\frac{\partial \omega(\mathbf{r})}{\partial x} \left\{ \sigma^e_{s11} \frac{\partial \phi^e_s}{\partial x} + \sigma^e_{s12} \frac{\partial \phi^e_s}{\partial y} + \sigma^e_{s13} \frac{\partial \phi^e_s}{\partial z} \right\} \right. \\
&\quad + \frac{\partial \omega(\mathbf{r})}{\partial y} \left\{ \sigma^e_{s21} \frac{\partial \phi^e_s}{\partial x} + \sigma^e_{s22} \frac{\partial \phi^e_s}{\partial y} + \sigma^e_{s23} \frac{\partial \phi^e_s}{\partial z} \right\} \\
&\quad \left. + \frac{\partial \omega(\mathbf{r})}{\partial z} \left\{ \sigma^e_{s31} \frac{\partial \phi^e_s}{\partial x} + \sigma^e_{s32} \frac{\partial \phi^e_s}{\partial y} + \sigma^e_{s33} \frac{\partial \phi^e_s}{\partial z} \right\} \right] dv \\
&= \int\int\int_{V^e} \omega(\mathbf{r}) \nabla \cdot \mathbf{j}_s(\mathbf{r}) dv,
\end{aligned} \tag{19}$$

where σ^e_{sij} denotes the element in row i and column j of the conductivity tensor $\bar{\bar{\sigma}}^e_s$. The unknown potential at a point inside the eth element is interpolated using the set of four Lagrange polynomials $n^e_j(\mathbf{r})$,

$$\phi^e(\mathbf{r}) = \sum_{j=1}^{4} \phi^e_j n^e_j(\mathbf{r}), \tag{20}$$

where ϕ^e_j is the potential at the jth node of the eth element.

The Lagrange polynomials are also used as the weighting function $\omega(\mathbf{r})$. Substituting equation 20 into equation 19 and replacing $\omega(\mathbf{r})$ by $n^e_i(\mathbf{r})$ yields

$$\begin{pmatrix} m^e_{11} & m^e_{12} & m^e_{13} & m^e_{14} \\ m^e_{21} & m^e_{22} & m^e_{23} & m^e_{24} \\ m^e_{31} & m^e_{32} & m^e_{33} & m^e_{34} \\ m^e_{41} & m^e_{42} & m^e_{43} & m^e_{44} \end{pmatrix} \begin{pmatrix} \phi^e_{s1} \\ \phi^e_{s2} \\ \phi^e_{s3} \\ \phi^e_{s4} \end{pmatrix} = \begin{pmatrix} q^e_1 \\ q^e_2 \\ q^e_3 \\ q^e_4 \end{pmatrix}, \tag{21a}$$

where

$$\begin{aligned}
m^e_{ij} = \int\int\int_{V^e} &\left[\frac{\partial n^e_i(\mathbf{r})}{\partial x} \left\{ \sigma^e_{s11} \frac{\partial n^e_j(\mathbf{r})}{\partial x} + \sigma^e_{s12} \frac{\partial n^e_j(\mathbf{r})}{\partial y} \right. \right. \\
&\left. + \sigma^e_{s13} \frac{\partial n^e_j(\mathbf{r})}{\partial z} \right\} + \frac{\partial n^e_i(\mathbf{r})}{\partial y} \left\{ \sigma^e_{s21} \frac{\partial n^e_j(\mathbf{r})}{\partial x} + \sigma^e_{s22} \frac{\partial n^e_j(\mathbf{r})}{\partial y} \right. \\
&\left. + \sigma^e_{s23} \frac{\partial n^e_j(\mathbf{r})}{\partial z} \right\} + \frac{\partial n^e_i(\mathbf{r})}{\partial z} \left\{ \sigma^e_{s31} \frac{\partial n^e_j(\mathbf{r})}{\partial x} + \sigma^e_{s32} \frac{\partial n^e_j(\mathbf{r})}{\partial y} \right. \\
&\left. \left. + \sigma^e_{s33} \frac{\partial n^e_j(\mathbf{r})}{\partial z} \right\} \right] dv,
\end{aligned} \tag{21b}$$

and

$$q^e_i = \int\int\int_{V^e} n^e_i(\mathbf{r}) \nabla \cdot \mathbf{j}_s(\mathbf{r}) dv.$$

Again, equation 21a is considered local because it comes from each tetrahedral element. Using the node connectivity information, these local matrix equations for the individual elements are assembled into a single global matrix equation for the secondary potential. Once the secondary potentials at all nodes are calculated, one can easily determine the electric field vectors along the edges of each tetrahedral element. These electric fields provide the initial values for equations 12a and 12b when a step-off source waveform is used. Once the electric fields are calculated, the magnetic fields can be easily interpolated using Faraday's law (Newman and Alumbaugh, 1995).

NUMERICAL IMPLEMENTATION APPROACH

The most expensive part of our FE computation is advancing the solution to equations 12a or 12b in time. To mitigate this potentially high computational cost, we use the fact that matrix **D** of equations 12a and 12b is a function of Δt; for a given Δt, the elements of matrix **D** do not vary in time. Therefore, matrix **D** should be computed within a time-stepping loop only once. If a direct solver is used with a constant Δt, the matrix needs to be factorized into corresponding lower and upper triangular matrices **L** and **U** only once. Eventually, after the explicit factorization, the computational cost in every time step reduces to that of forward and backward substitutions, resulting in a much cheaper computational cost per time step. When an iterative solver is used to solve equation 12a or 12b, a preconditioner also needs to be computed only once if Δt is constant.

In this rendition of the algorithm, we choose a direct solver (Davis, 2006) over an iterative solver because the use of an iterative solver for equation 1 results in poor convergence and spurious solutions in the static limit (Alumbaugh et al., 1996; Smith, 1996; Dyczij-Edlinger et al., 1998; Newman and Alumbaugh, 2002). Before a direct factorization starts, the matrix is reordered to minimize fill-ins in the resulting triangular matrices (Demmel, 1997). Minimizing fill-ins is critically important to reduce the computational and memory costs. Once the factorization generates triangular matrices, they are repeatedly used to advance the solution of the equation 12a or 12b via forward and backward substitutions.

Although using the constant Δt eliminates the necessity of refactorizing the FE matrix in every time step, the constant Δt is not the best choice for simulating diffusive TEM responses, especially over a large range of time (e.g., from 10^{-6} to 10^{2} s). For such a diffusion problem, a very small Δt is required in early time to resolve the broad frequency spectrum of the induced TEM fields. However, as the high-frequency components of the TEM fields are more rapidly attenuated in time, one can take increasingly larger time steps and thus can advance the solution quickly without affecting the accuracy. Therefore, it is desirable to change Δt as an efficient problem-solving strategy. If, however, the algorithm is allowed to change Δt at every time step in an attempt to determine and use the optimal Δt, our simulation, at least in a serial computing environment, shows that the effort entails significant computational overhead, resulting in a net loss of the computational benefits from a larger Δt.

In our FETD algorithm, we attempt to double Δt every m time steps, where m is an input parameter. If an earth model is conductive and attenuates the EM fields quickly, a smaller m is chosen; if an earth model is somewhat resistive, a larger m needs to be chosen. When the FETD algorithm tries to switch a time-step size from, say, Δt to $2\Delta t$, the electric fields are computed at a given time using the two time steps. Then the difference between the two sets of the electric field solutions is compared. If the difference is smaller than a prescribed tolerance, $2\Delta t$ is accepted as a new time-step size. If the tolerance criterion is not satisfied, the algorithm rejects $2\Delta t$ and continues using the current Δt. However, the triangular matrix for $2\Delta t$ is stored for future use after another m time steps. For brevity, we call this approach the adaptive time-step doubling method.

VALIDATION AND PERFORMANCE ANALYSIS

So far, we have described the details of our FETD algorithm and its numerical implementation. To demonstrate the accuracy and performance of our algorithm, its serial implementation, named FETDEM3D, is written in MATLAB 7.5, from which several external routines are also called. The MATLAB portion of FETDEM3D mainly includes FE preprocessing tasks, whereas the external routines are responsible for the main FE computations; the direct matrix factorization is performed using SuiteSparse 3.2 and other auxiliary routines authored by Davis (2006); fill-reducing ordering of sparse matrices is performed using METIS 4.0 (Karypis and Kumar, 1999); and 3D FE discretization is carried out using the Delaunay algorithm and other algorithms in COMSOL 2008 Multiphysics 3.5a software. The FETD computations presented here were carried out on a single-core Opteron 875 2.2 GHz with 8-GB memory running Red Hat Linux.

The results are compared with 1D analytic or the 3D FDTD solutions of Commer and Newman (2004). Note that the analytic solution first computes the frequency-domain responses at a selected number of frequencies and then converts the responses to the time domain using inverse fast-Fourier-transform routines. Although our FETD algorithm can simultaneously handle multiple arbitrarily configured electric dipoles that are excited with various source waveforms over general anisotropic media, only single step-off electric dipole responses over isotropic media are considered in this section for comparison and verification purposes.

Homogeneous seafloor model

The first example is a simple marine TD-CSEM simulation. Figure 2 illustrates a homogeneous seafloor model with a 400-m-deep seawater column. A 250-m-long electric dipole source is placed 50 m above the seafloor. Its ramp-off time is set to 0.01 (s). Eight receivers are placed on the seafloor from $x = 1$ to 8 km along $y = 0$. To ensure both numerical stability and accuracy, the resistivity of the air is empirically set to 10,000 Ωm.

The boundaries of the model are extended to 100 km from the model center to eliminate possible artificial boundary effects at the receiver positions. To discretize the model economically, element growth factors ranging from 1.5 to 2.0 are used in most areas. However, inside the seawater column, which has a thickness of 400 m, tetrahedral elements are not allowed to grow rapidly in the x- and y-directions so as not to skew the elements too much. Consequently, the model is discretized into a somewhat large number (108,540) of tetrahedral elements, generating 125,883 unknowns.

Figure 3 shows the inline and broadside responses over the model and their relative percentage errors with respect to the analytic solutions. Overall good agreement is observed for both solutions. As time stepping continues, the oscillations of percentage errors gradually increase due to the error migration from early to late time but remain within acceptable levels. Note that the z-components of the

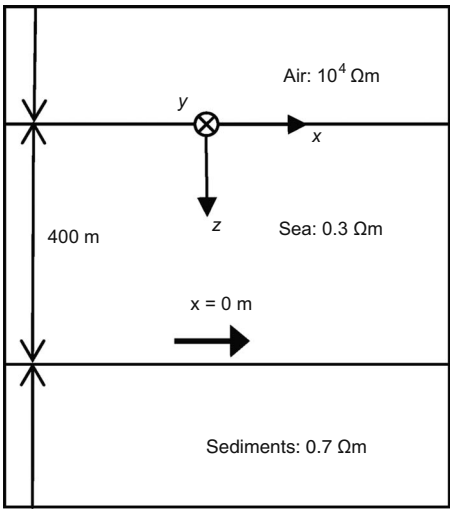

Figure 2. The x-z section ($y = 0$ m) of the homogeneous seafloor model. The black horizontal arrow is an electric dipole source directed along the x-axis. Its center is placed at (0 m, 0 m, 350 m).

electric fields ($\mathbf{E}_z$) are more vulnerable to the error migration than the x-components of the electric fields ($\mathbf{E}_x$). When an x-oriented electric dipole source is simulated, such an error pattern is observed repeatedly in our modeling experiments. We believe that this is because the amplitudes of $\mathbf{E}_z$ are an order of magnitude smaller than those of $\mathbf{E}_x$ and therefore are more easily contaminated with numerical noises. The y-components of the electric fields ($\mathbf{E}_y$) clearly show typical sign reversals observed in the broadside configuration. In the vicinity of the sign reversals, the percentage errors sharply increase but quickly reduce to a reasonable level, verifying the accuracy of the FETD algorithm.

Note that the analytic solutions for the z-components of magnetic fields ($\mathbf{B}_z$) are computed first, and then their time derivatives ($\partial \mathbf{B}_z / \partial t$) are numerically approximated. The approximations are somewhat noisy in a very early time range (e.g., from 0.01 to 0.05 s) due to catastrophic cancellation and thus are not plotted in that time range. The

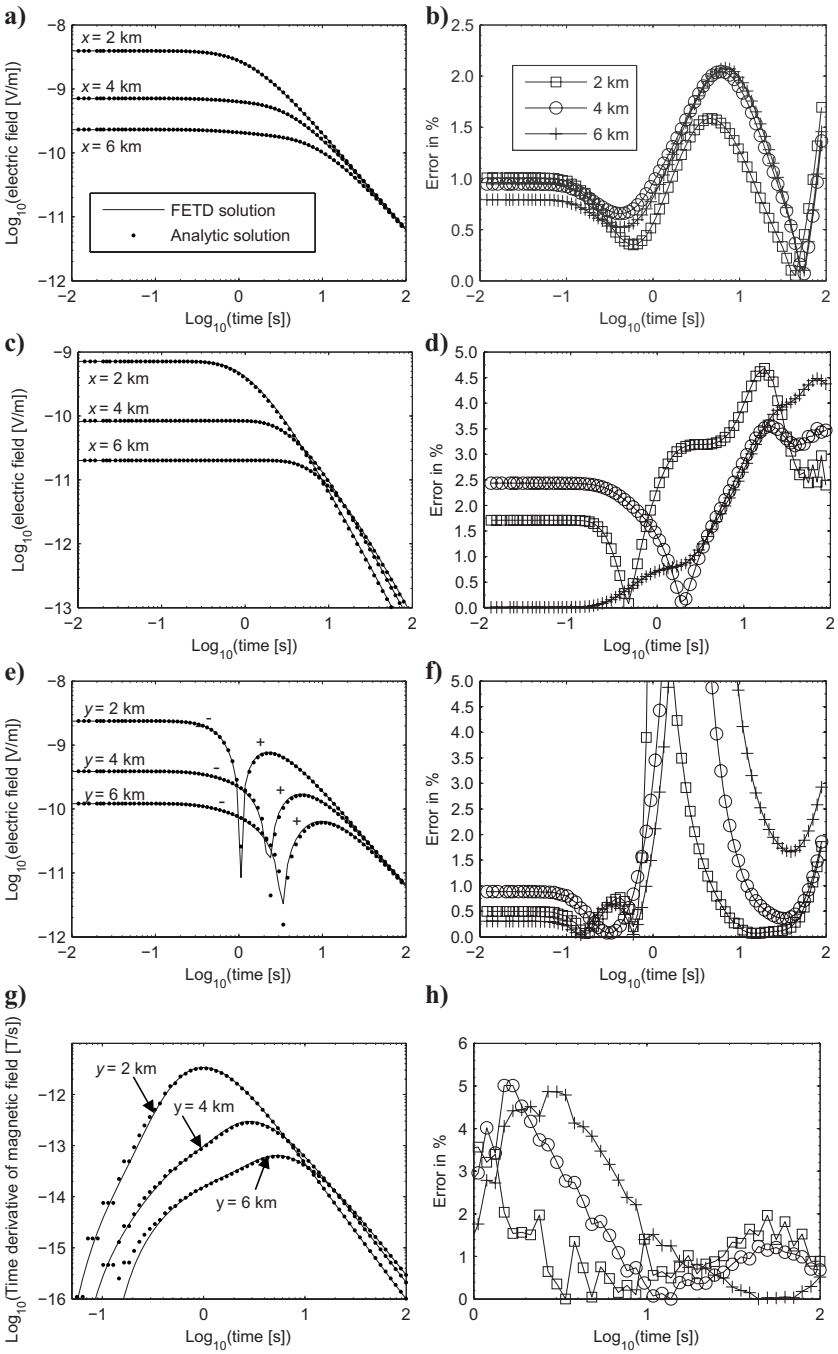

Figure 3. The TD-CSEM inline and broadside responses for selected receiver positions over the model shown in Figure 2. The left column contains the EM fields; the right column contains the percentage difference (e.g., error) between the analytic and the FETD solutions. (a) Inline $\mathbf{E}_x$. (b) Relative errors (%) in inline $\mathbf{E}_x$. (c) Inline $\mathbf{E}_z$. (d) Relative errors (%) in inline $\mathbf{E}_z$. (e) Broadside $\mathbf{E}_y$. (f) Relative errors (%) in broadside E_y. (g) Broadside ($\partial \mathbf{B}_z / \partial t$). (h) Relative errors (%) in broadside ($\partial \mathbf{B}_z / \partial t$).

noise resulting from the numerical approximation is still seen as a stair-step pattern in the early time (e.g., from 0.05 to 1 s) in Figure 3g. However, in intermediate and late time (from 1 to 100 s), the $dB_z dt$ curves of both analytic and FETD solutions show excellent agreement with low percentage errors (e.g., $<2\%$), ensuring the accuracy of the FETD algorithm.

Figure 4 summarizes the performance and effectiveness of the adaptive time-step doubling method. Without the method, the simulation took 16.2 hours with 50,000 time steps to complete the simulation. In contrast, when the doubling method was used, the simulation was completed in just 36 minutes with 1393 time steps. The time-step doubling procedures were applied eight times, which implies that the factorization of matrix **D** in equation 12b is performed only nine times to complete the simulation.

Seafloor model with resistive layer

In the next example, a 100-m-thick and 100-Ωm resistive layer (e.g., oil or CO_2 reservoir) is inserted into the first model (Figure 2) at a depth of 1 km from the seafloor. The other simulation parameters are kept the same. The model is discretized into 209,252 tetrahedral elements, generating 243,543 unknowns along the edges of the tetrahedral elements. Again, a large number of tetrahedral elements are required to discretize the thin 1D reservoir. It took 68 minutes to simulate this seafloor model with eight time-step doubling procedures. The inline and broadside electric field responses over the model are shown in Figure 5. The FETD solutions agree well with the analytic solutions.

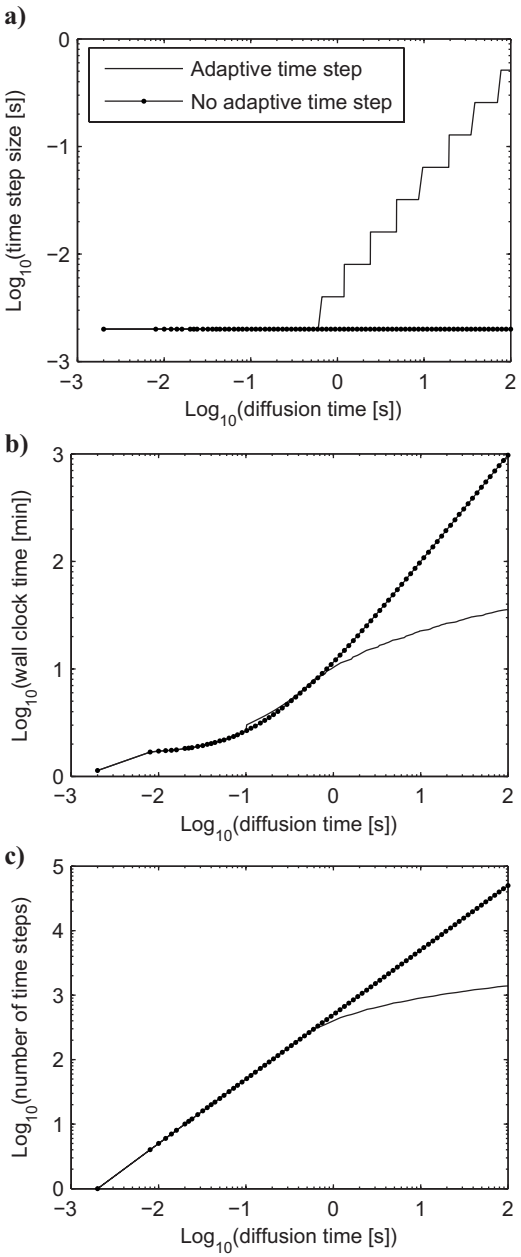

Figure 4. Comparison of computational efficiency in the model shown in Figure 2 with and without the time-step doubling method. (a) The evolution of a time-step size as a function of diffusion time. (b) The wall clock time as a function of diffusion time. (c) The number of time steps as a function of diffusion time. The diffusion time is the time scale in which the EM diffusion phenomena occur.

3D gas reservoir model

The next example is a 3D resistive gas reservoir shown in Figure 6. In this model, the resistivity of the air is set to 10^8 Ωm, which is four orders of magnitude larger than that of the air in the previous models. However, our numerical modeling experiments indicate that such a highly resistive air layer is required to ensure accurate solutions when sources and receivers are placed at the air-earth interface. As a side note, we were able to set the resistivity of the air to a maximum 10^{12} Ωm when a direct solver is used. Beyond the limit, matrix **D** in equations 12a and 12b becomes too poorly conditioned, resulting in inaccurate and unstable solutions.

The inline TD-CSEM responses over the gas reservoir are simulated using both FDTD and FETD algorithms. A 250-m-long electric

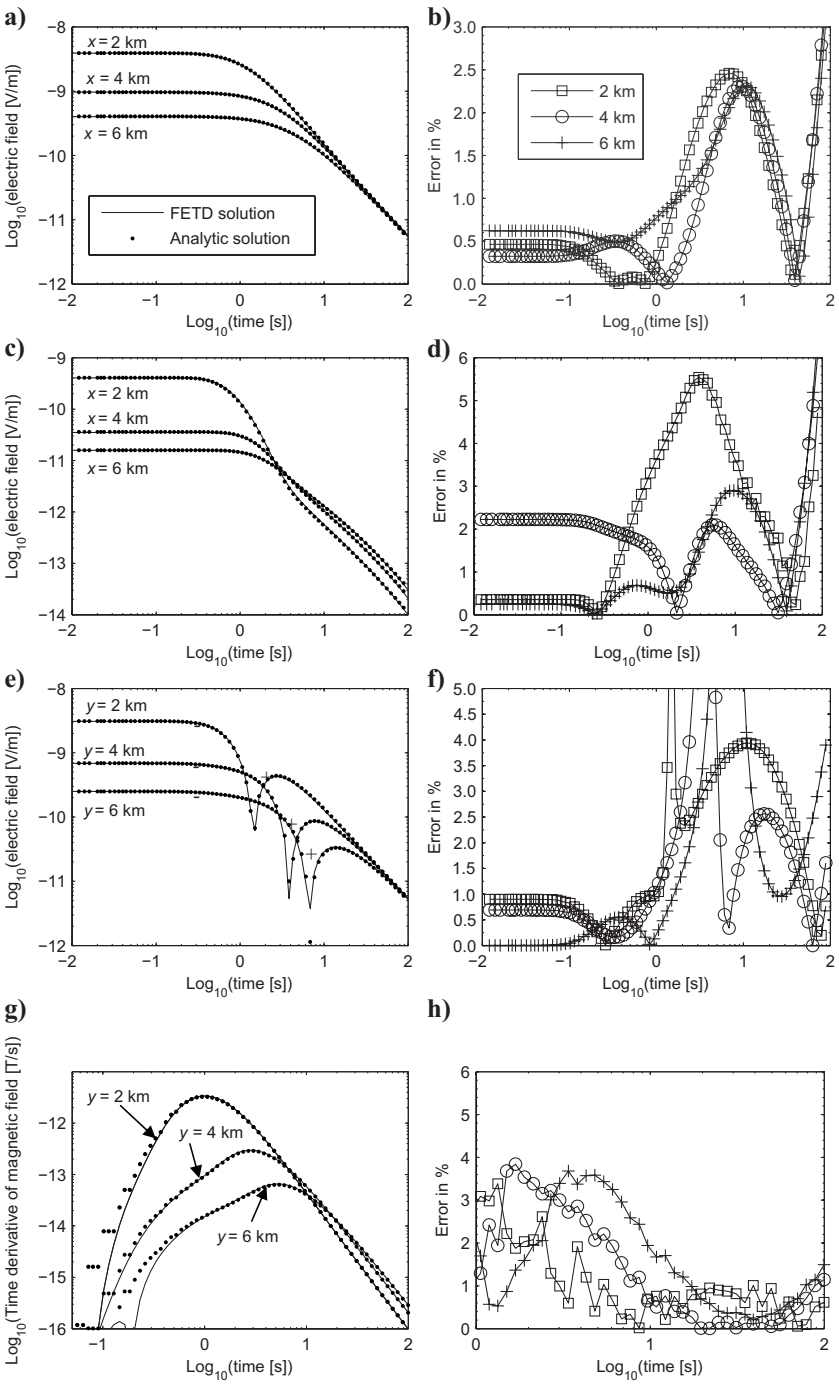

Figure 5. The TD-CSEM inline and broadside responses for the three receiver positions over the model shown in Figure 2 with the 100-m-thick reservoir at 1-km depth below the seafloor. The left column contains the EM fields; the right column contains the percentage difference (e.g., error) between the analytic and the FETD solutions. (a) Inline $\mathbf{E}_x$. (b) Relative errors (%) in inline $\mathbf{E}_x$. (c) Inline $\mathbf{E}_z$. (d) Relative errors (%) in inline $\mathbf{E}_z$. (e) Broadside $\mathbf{E}_y$. (f) Relative errors (%) in broadside $\mathbf{E}_y$. (g) Broadside $(\partial \mathbf{B}_z / \partial t)$. (h) Relative errors (%) in broadside $(\partial \mathbf{B}_z / \partial t)$.

dipole whose ramp-off time is set to 10^{-4} s is placed at the center of the model. The FDTD modeling results for the model are computed using the 3D FDTD solution (Commer and Newman, 2004). The FDTD model consists of $139 \times 99 \times 71$ grid cells in the x-, y-, and z-directions with the computational domain boundaries at 10 km from the source. The FDTD model has 2,931,093 unknowns. In contrast, the FETD algorithm discretizes the model into 114,116 tetrahedral elements, generating 131,741 unknowns. Note that the total number of grid cells required for the FDTD model is nearly nine times larger than that for the FETD model. The comparison above illustrates the fact that an FETD mesh can economically discretize a large computational domain with a relatively small number of unknowns.

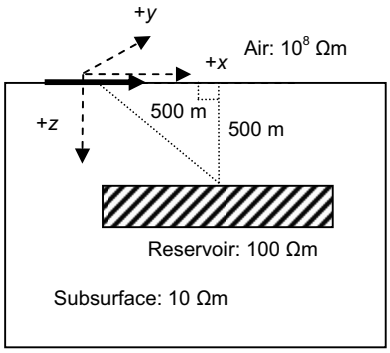

Figure 6. The 3D gas reservoir model. The thick black arrow on the air-earth interface is a 250-m-long electric dipole source. The size of the reservoir is $600 \times 600 \times 100$ m in x-, y-, and z-directions, respectively. Its axis base point is (200 m, −300 m, 600 m).

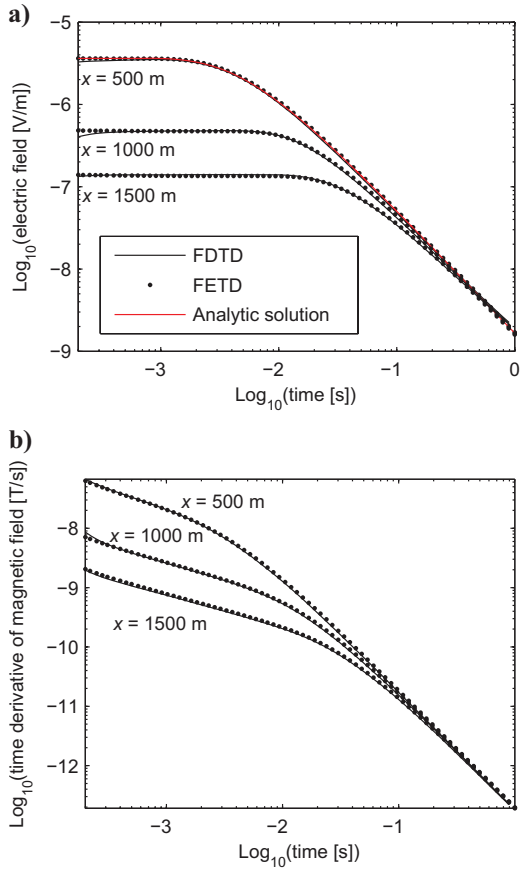

Figure 7. The TD-CSEM inline responses at three receiver positions over the model shown in Figure 6. The analytic solution for the same earth model without the 3D gas reservoir is computed only for the electric field at $x = 500$ m. (a) $\mathbf{E}_x$. (b) $(\partial \mathbf{B}_z / \partial t)$.

The cross-sectional view ($y = 0$) of the FETD mesh used for the model is shown in Figure 1. In the FETD mesh design, we deliberately use very fine elements around the source so as to accurately resolve the very early time behavior of the TEM fields for verification purposes even though the early time TEM fields do not convey useful information about the 3D reservoir. Note that such a mesh generation is feasible only in FE modeling because fine meshes in the center of the model do not have to extend to the computational boundaries of the FETD model (Key and Weiss, 2006). The mesh boundary of the FETD model is 30 km away from the source to ensure accurate solutions at very late time. It took 53 minutes to complete the FETD simulation with 1559 time steps when the adaptive time-step doubling method was used.

The simulation results from the FETD and FDTD methods are plotted in Figure 7. Although the curves for each receiver position agree well with each other at most times, slight differences in the electric fields are observed in very early and late time. To evaluate the degree of accuracy of both solutions, we adapt the methodology of Commer and Newman (2004); an analytic solution over the same earth model without the 3D gas reservoir is calculated at the shortest source-receiver offset (e.g., $x = 500$ m) and compared with the corresponding FDTD and FETD solutions. Because the influence of the 3D reservoir at the shortest offset can be assumed very small, the closer agreement of the FETD solution with the analytic solution in Figure 7 verifies the accuracy of the FETD solutions. Therefore, we safely conclude that the FETD and FDTD solutions will agree with each other more closely at very early time if the grid for the FDTD solutions is carefully refined.

Dipping seafloor model

Marine TD-CSEM responses, illustrated in Figure 8, are calculated for a gently dipping 2D seafloor of 4° degrees with and without a 3D hydrocarbon reservoir. To elucidate the effects of the slope on the

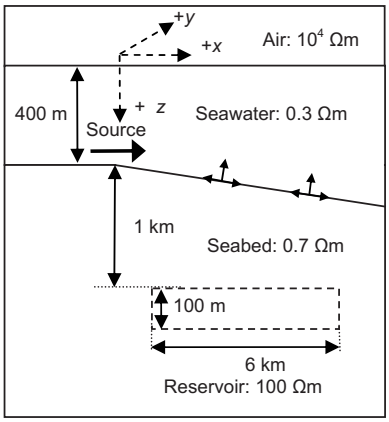

Figure 8. A gently dipping seafloor structure with and without a reservoir: ⊥ with arrows indicates EM receivers. The dipping angle of the seafloor is 4°. A 250-m-long electric dipole source is placed 50 m above the seafloor. The reservoir position is outlined with the dashed box. The size of the reservoir is $6 \times 6 \times 0.1$ km in the x-, y- and z-directions, respectively. Its axis base point is (1 km, −3 m, 1500 m).

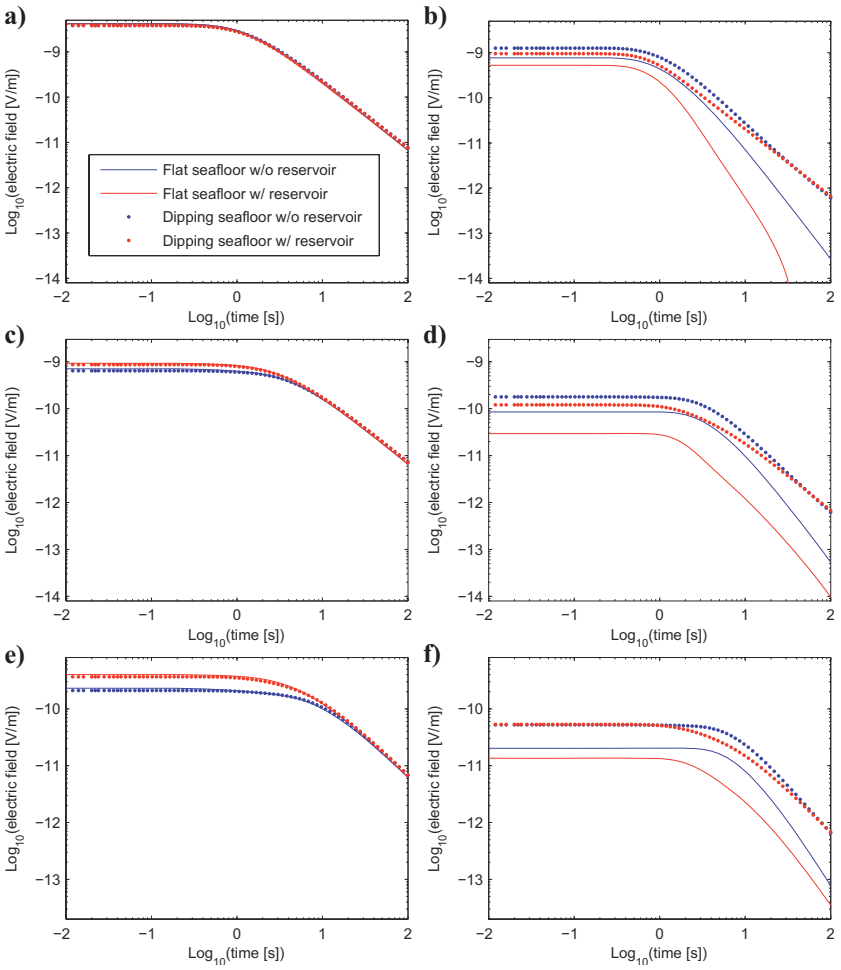

Figure 9. Inline TD-CSEM responses over the model shown in Figure 8. (a) $\mathbf{E}_x$ at $x = 2$ km. (b) $\mathbf{E}_z$ at $x = 2$ km. (c) $\mathbf{E}_x$ at $x = 4$ km. (d) $\mathbf{E}_z$ at $x = 4$ km. (e) $\mathbf{E}_x$ at 6 km. (f) $\mathbf{E}_z$ at $x = 6$ km.

marine TD-CSEM method, a flat seafloor model with and without the same hydrocarbon reservoir is also simulated. The flat seafloor model has a uniform 400-m-thick seawater column. The dipping and flat seafloor models are discretized into 165,528 tetrahedral elements with 191,780 unknowns and 127,046 tetrahedral elements with 146,871 unknowns, respectively. The simulations are completed in 65 minutes and 41 minutes, respectively.

The inline E_x and E_z responses for the flat and dipping seafloor models with and without the reservoir are compared each other at three receiver positions in Figure 9. The noticeable differences observed in Figure 9 can be interpreted as the combination of the following factors. First, receivers on the slope have a thicker water column above them as the source-receiver offset gradually increases. As a result, they record a different level of the airwave effect from those on the flat seafloor. Second, receivers on the slope measure stronger galvanic effects than those on the flat seafloor because of their shorter distance from the resistive reservoir. Third, receivers on the slope are tilted toward the slope. Thus, the x- and z-components of the receivers do not point in the same directions as the x- and z-components of receivers on the flat seafloor. Because the amplitudes of horizontal electric fields are much larger than those of vertical electric fields, the tilt of a receiver's coordinate system due to the slope has a significant impact, especially on the vertical electric field measurements. In short, a gently dipping simple 2D seafloor structure can cause significant effects on the TD-CSEM measurements. As demonstrated above, seafloor bathymetry needs to be modeled with special care.

CONCLUSIONS

We have presented an efficient 3D FETD algorithm to simulate EM diffusion phenomena excited by electric dipole sources. The algorithm is especially useful for modeling complex topography and reservoir geometry. Comparisons with analytic and 3D FDTD solutions demonstrate the accuracy and efficiency of our 3D FETD algorithm. The FETD algorithm directly solves transient electric fields by applying Galerkin's method with homogeneous Dirichlet boundary conditions to the electric field diffusion equation. To compute initial electric fields over an arbitrary conductivity earth model for a step-off source waveform, the secondary potential method is used to solve Poisson's equation.

The FETD algorithm uses an implicit backward Euler scheme to retain numerical stability with a larger time-step size that helps to accelerate the FETD solution, especially in late time. The inherent high-computational effort associated with solving the resultant FETD matrix-vector equation in every time step is mitigated by refactorizing the FETD matrix only when a time-step size is changed. By adaptively doubling a time-step size at intervals, the FETD algorithm trades off the computational cost in refactorizing the FETD matrix for the faster advance in FETD solutions. The adaptive doubling of the time step plays an important role in speeding up the

FETD computation, especially in a marine TD-CSEM simulation wherein an EM diffusion process occurs slowly until very late time due to the high electrical conductivities of the model.

ACKNOWLEDGMENTS

This work was carried out using the computing facilities at the Center of Computational Earth and Environmental Science, Stanford University. Um is supported by the Mrs. C. J. Belani Fellowship for Computational Geosciences from the Center of Computational Earth and Environmental Science and by the Chevron Stanford Graduate Fellowship. We express our gratitude to Nestor Cuevas at Schlumberger-EMI Technology Center for help with the analytic solutions, Michael Commer at Lawrence Berkeley National Laboratory for the 3D FDTD computations, and Yuguo Li at Scripps Institution of Oceanography (University of California at San Diego) for valuable comments on FEDC computations. We also thank the anonymous reviewers and editor for their useful suggestions to improve this paper.

REFERENCES

Alumbaugh, D., G. Newman, L. Prevost, and J. Shadid, 1996, Three-dimensional wideband electromagnetic modeling on massively parallel computers: Radio Science, **31**, 1–23.

Biro, O., and K. Preis, 1989, On the use of the magnetic vector potential in the finite element analysis of three-dimensional eddy currents: IEEE Transactions on Magnetics, **25**, 3145–3159.

Börner, R.-U., O. G. Ernst, and K. Spitzer, 2008, Fast 3D simulation of transient electromagnetic fields by model reduction in the frequency domain using Krylov subspace projection: Geophysical Journal International, **173**, 766–780.

Bossavit, A., 1988, Whitney forms: A class of finite elements for three-dimensional computations in electromagnetism: IEEE Physical Science, Measurement and Instrumentation, Management and Education Reviews, **135**, 493–500.

Cangellaris, A., C. Lin, and K. Mei, 1987, Point-matched time domain finite element methods for electromagnetic radiation and scattering: IEEE Transactions on Antennas and Propagation, **35**, 1160–1173.

Commer, M., and G. Newman, 2004, A parallel finite-difference approach for 3D transient electromagnetic modeling with galvanic sources: Geophysics, **69**, 1192–1202.

Davis, T., 2006, Direct methods for sparse linear systems: Society for Industrial and Applied Mathematics.

Demmel, J., 1997, Applied numerical linear algebra: Society for Industrial and Applied Mathematics.

Dey, A., and H. F. Morrison, 1978, Resistivity modeling for arbitrarily shaped three-dimensional structures: Geophysics, **44**, 753–780.

Dyczij-Edlinger, R., C. Peng, and J. Lee, 1998, A fast vector-potential method using tangentially continuous vector finite elements: IEEE Transactions on Microwave Theory and Techniques, **46**, 863–868.

Everett, M. E., and R. N. Edwards, 1992, Transient marine electromagnetics: The 2.5-D forward problem: Geophysical Journal International, **113**, 545–561.

Gedney, S., and U. Navsariwala, 1995, An unconditionally stable implicit finite-element time-domain solution of the vector wave equation: IEEE Microwave Guided Wave Letters, **5**, 332–334.

Gockenbach, M. S., 2002, Partial differential equations: Society for Industrial and Applied Mathematics.

Goldman, Y., C. Hubans, S. Nocoletis, and S. Spitz, 1985, A finite-element solution for the transient electromagnetic response of an arbitrary two-dimensional resistivity distribution: Geophysics, **51**, 1450–1461.

Haber, E., U. Ascher, and D. Oldenburg, 2004, Inversion of 3D electromagnetic data in frequency and time domain using an inexact all-at-once approach: Geophysics, **69**, 1216–1228.

Hairer, E., and G. Wanner, 1991, Solving ordinary differential equations 2: Stiff and differential-algebraic problems: Springer-Verlag.

Hördt, A., and M. Müller, 2000, Understanding LOTEM data from mountainous terrain: Geophysics, **65**, 1113–1123.

Jin, J., 2002, The finite element method in electromagnetics, second edition: John Wiley and Sons.

Karypis, G., and V. Kumar, 1999, A fast and high quality multilevel scheme for partitioning irregular graphs: SIAM Journal on Scientific Computing, **20**, 359–392.

Key, K., and C. Weiss, 2006, Adaptive finite-element modeling using unstructured grids: The 2D magnetotelluric example: Geophysics, **71**, no. 6, G291–G299.

Lee, J., R. Lee, and A. Cangellaris, 1997, Time-domain finite-element methods: IEEE Transactions on Antennas and Propagation, **35**, 430–442.

Li, Y., and K. Spitzer, 2002, Three-dimensional DC resistivity forward modeling using finite elements in comparison with finite-difference solutions: Geophysical Journal International, **151**, 924–934.

———, 2005, Finite element resistivity modeling for three-dimensional structures with arbitrary anisotropy: Physics of the Earth and Planetary Interiors, **150**, 15–27.

Lowry, T., M. Allen, and P. Shive, 1989, Singularity removal: A refinement of resistivity modeling techniques: Geophysics, **54**, 766–774.

Nédélec, J.-C., 1980, Mixed finite elements in R^3: Numerische Mathematik, **35**, 315–341.

———, 1986, A new family of mixed elements in R^3: Numerische Mathematik, **50**, 57–81.

Newman, G., and D. Alumbaugh, 1995, Frequency-domain modeling of airborne electromagnetic responses using staggered finite differences: Geophysical Prospecting, **43**, 1021–1042.

———, 2002, Three-dimensional induction logging problems: Part 2 — A finite-difference solution: Geophysics, **67**, 484–491.

Rieben, R., and D. White, 2006, Verification of high-order mixed finite-element solution of transient magnetic diffusion problems: IEEE Transactions on Magnetics, **42**, 25–39.

Smith, T., 1996, Conservative modeling of 3-D electromagnetic fields: Part 2 — Biconjugate gradient solution and an accelerator, Geophysics, **61**, 1319–1324.

Taflove, A., 1980, Application of the finite-difference time-domain method to sinusoidal steady-state electromagnetic penetration problems: IEEE Transactions on Electromagnetic Compatibility, **22**, 191–202.

Taflove, A., and S. Hagness, 2005, Computational electromagnetics, 3rd ed.: Artech House.

Wang, T., and G. W. Hohmann, 1993, A finite-difference, time-domain solution for three-dimensional electromagnetic modeling: Geophysics, **58**, 797–809.

Whitney, H., 1957, Geometric integration theory: Princeton University Press.

Yee, K., 1966, Numerical solution of initial boundary value problems involving Maxwell's equations in isotropic media: IEEE Transactions on Antennas and Propagation, **14**, 302–307.

Zhu, Y., and A. Cangellaris, 2006, Multigrid finite element methods for electromagnetic field modeling: Wiley-IEEE Press.